

Theoretical and Experimental Studies of ion Transport in Mixed Polyanion Solid Electrolytes

Zeyu Deng

National University of Singapore <https://orcid.org/0000-0003-0109-9367>

Tara Mishra

National University of Singapore

Eunike Mahayoni

Université de Picardie Jules Verne

Qianli Ma

Forschungszentrum Jülich <https://orcid.org/0000-0002-4709-4927>

Olivier Guillon

Forschungszentrum Juelich GmbH, Institute of Energy and Climate Research IEK-1

Jean-Noel Chotard

University of Picardie Jules Verne <https://orcid.org/0000-0002-9867-7954>

Vincent Seznec

<https://orcid.org/0000-0001-5233-5943>

Anthony K. Cheetham

University of Cambridge <https://orcid.org/0000-0003-1518-4845>

Christian Masquelier

Univ. Picardie Jules Verne

Gopalakrishnan Sai Gautam

Massachusetts Institute of Technology <https://orcid.org/0000-0002-1303-0976>

Pieremanuele Canepa (✉ pcanepa@nus.edu.sg)

National University of Singapore <https://orcid.org/0000-0002-5168-9253>

Article

Keywords: ion transport, polyanion mixing, NASICON

Posted Date: December 1st, 2021

DOI: <https://doi.org/10.21203/rs.3.rs-1102507/v1>

License:   This work is licensed under a Creative Commons Attribution 4.0 International License.

[Read Full License](#)

Version of Record: A version of this preprint was published at Nature Communications on August 2nd, 2022. See the published version at <https://doi.org/10.1038/s41467-022-32190-7>.

Theoretical and Experimental Studies of ion Transport in Mixed Polyanion Solid Electrolytes

Zeyu Deng,^{1*} Tara P. Mishra,^{1,2} Eunike Mahayoni,^{3,4,5} Qianli Ma,⁶ Olivier Guillon,^{6,7}
Jean-Noël Chotard,^{3,4,5} Vincent Seznec,^{3,4,5} Anthony K. Cheetham,¹ Christian
Masquelier^{3,4,5} Gopalakrishnan Sai Gautam,⁸ and Pieremanuele Canepa^{1,2,9#}

¹Department of Materials Science and Engineering, National University of Singapore, Singapore
117575, Singapore

²Singapore-MIT Alliance for Research and Technology, 1 CREATE Way, 10-01 CREATE Tower,
Singapore 138602, Singapore

³Laboratoire de Réactivité et de Chimie des Solides (LRCS), CNRS UMR 7314, Université de
Picardie Jules Verne, 80039 Amiens Cedex, France.

⁴RS2E, Réseau Français sur le Stockage Electrochimique de l'Energie, FR CNRS 3459, F-80039
Amiens Cedex 1, France.

⁵ALISTORE-ERI European Research Institute, FR CNRS 3104, Amiens, F-80039 Cedex 1, France.

⁶Forschungszentrum Jülich GmbH, Institute of Energy and Climate Research, Materials Synthesis
and Processing (IEK-1), 52425 Jülich, Germany

⁷Helmholtz-Institute Münster, c/o Forschungszentrum Jülich GmbH, 52425 Jülich, Germany

⁸Department of Materials Engineering, Indian Institute of Science, Bengaluru, 560012, Karnataka,
India

⁹Chemical and Biomolecular Engineering, National University of Singapore, 4 Engineering Drive 4,
Singapore, 117585, Singapore.

Corresponding authors: *msedz@nus.edu.sg and #pcanepa@nus.edu.sg

Abstract

Lithium and sodium (Na) mixed polyanion solid electrolytes for all-solid-state batteries display some of the highest ionic conductivities reported to date. However, the effect of polyanion mixing on ion transport properties is still debated. Here, we focus on $\text{Na}_{1+x}\text{Zr}_2\text{Si}_x\text{P}_{3-x}\text{O}_{12}$ ($0 \leq x \leq 3$) NASICON electrolyte to elucidate the role of polyanion mixing on Na-transport properties. Although there is a large body of data available on this NASICON system, transport properties extracted from experiments or theory vary by orders of magnitude, signifying the need to bridge the gap between different studies. Here, more than 2,000 distinct *ab initio*-based kinetic Monte Carlo simulations have been used to map the statistically vast compositional space of NASICON over an unprecedented time range and spatial resolution and across a range of temperatures. We performed impedance spectroscopy of samples with varying Na compositions revealing that the highest ionic conductivity ($\sim 0.1 \text{ S cm}^{-1}$) is achieved in $\text{Na}_{3.4}\text{Zr}_2\text{Si}_{2.4}\text{P}_{0.6}\text{O}_{12}$, in line with our predictions ($\sim 0.2 \text{ S cm}^{-1}$). Our predictions indicate that suitably doped NASICON compositions, especially with high silicon content, can achieve high Na^+ mobilities. Our findings are relevant for the optimization of mixed polyanion solid electrolytes and electrodes, including sulfide-based polyanion frameworks, which are known for their superior ionic conductivities.

Introduction

The reliability of rechargeable batteries and other energy storage devices depends on the fast delivery of ions between electrodes.¹⁻⁴ In rechargeable batteries, the safety and performance of electrolytes are as important as other battery components, such as electrodes. Solid-state batteries, where liquid electrolytes are replaced by solid fast-ion conductors, offer a promising pathway for safer commercial lithium-ion and prototypical sodium (Na)-ion batteries.⁴⁻⁶ Several solid electrolytes, such as the LiSiCON-type $\text{Li}_{4\pm x}\text{Si}_{1-x}\text{Z}_x\text{O}_4$ ($Z = \text{P}^{5+}, \text{Al}^{3+}, \text{Sn}^{4+}$ and/or Ge^{4+}),^{7,8} $\text{Li}_{10}\text{MP}_2\text{S}_{12}$ made from $\text{Li}_4\text{MS}_4:\text{Li}_3\text{PS}_4$ ($M = \text{Ge}^{4+}, \text{Sn}^{4+},$ and Si^{4+}),⁹⁻¹⁶ and $\text{Na}_{1+x}\text{Zr}_2\text{Si}_x\text{P}_{3-x}\text{O}_{12}$ (hereafter referred as NASICON),¹⁷⁻¹⁹ leverage mixed polyanion frameworks to attain some of the highest ionic conductivities (≈ 10 mS/cm) reported so far.⁴

Ion transport in mixed polyanion solid electrolytes has been investigated using both computation and experiments before.^{4,9,18,7,11} Yet transport properties measured from different techniques typically vary by orders of magnitude.²⁰ On one hand, averaged transport properties obtained from experiments, such as impedance spectroscopy, solid-state nuclear magnetic resonance, and quasi-elastic neutron scattering,^{4,6,16,21} may incorporate effects arising from defects and grain boundaries.²² On the other hand, classical or *ab initio* molecular dynamics (MD) studies perform “one shot” simulations on selected bulk structures, which may not be sufficiently representative in terms of longer time-scale transport processes as well as in the number of possible arrangements of different polyanions.^{2,3,23-25} Thus, there is a need to reconcile the measurements and simulations to guide the development and manufacturing of the next generation of solid electrolytes and their batteries.

In this study, we have selected the NASICON $\text{Na}_{1+x}\text{Zr}_2\text{Si}_x\text{P}_{3-x}\text{O}_{12}$ ($0 \leq x \leq 3$) electrolyte as an example to elucidate the role of polyanion mixing on the macroscopic

transport properties, including ionic diffusivity and conductivity. The choice of NASICON is justified by the large body of data available on this system since its discovery more than 40 years ago,^{17,18,26–29} making it easier to reconcile previous experimental and computational studies.

To capture the large statistical variance in transport properties introduced by mixed polyanions in NASICON samples, we developed a high-fidelity kinetic Monte Carlo (kMC) model bearing the accuracy of density functional theory (DFT) calculations. More than 2,000 distinct kMC simulations served to map the statistically vast compositional space of $\text{Na}_{1+x}\text{Zr}_2\text{Si}_x\text{P}_{3-x}\text{O}_{12}$ over an unprecedented time range – in the realm of milliseconds – and spatial resolution, with varying temperature.

First of all, our model reproduces existing measurements of Na-transport properties in NASICON, suggesting that a robust sampling of both the spatial and temporal axes is required in computations to accurately estimate these properties. The reproduction of measured Na-transport properties in NASICON also implies that our model correctly captures the collective nature of Na-transport, which is responsible for the high ionic conductivity observed in NASICON. Second, our simulations elucidate the impact of the thermodynamic forces driving the random distribution of PO_4^{3-} and SiO_4^{4-} groups in NASICON during synthesis (and subsequent thermal treatment) on the Na-ion transport. Third, our statistical insights can guide the selection of optimal doping and thermal treatment strategies to further improve the properties of NASICON electrolytes. For example, our analysis suggests that higher Na^+ conductivity in NASICON can be achieved by increasing the content of SiO_4^{4-} units in place of PO_4^{3-} moieties, while maintaining high Na content in the structure. Motivated by our computational findings, we have also synthesized and characterized selected compositions of the NASICON, which validates our predictions. These findings,

elaborated on NASICON electrolytes, are general and transferable to the study of ionic transport in other topical mixed-polyanion Li and Na solid electrolytes.

Results

Figure 1a depicts the crystal structure of NASICON, where red SiO_4/PO_4 tetrahedra share corners with two blue ZrO_6 octahedra forming the so-called “lantern units”. In the rhombohedral high-temperature NASICON structure ($R\bar{3}c$), there are two independent and partially occupied sodium sites, Na(1) and Na(2). The partial occupancy of these sites gives rise to the well-known high ionic conductivity in NASICON. A third interstitial Na site, known as Na(3), adjacent to Na(1) and Na(2) has been previously considered.^{30,31} However, Zhang *et al.*³² showed that Na(3) is negligibly occupied over a wide range of temperatures ($200 < T < 800$ °C) and less relevant for Na-transport in NASICON. The structural images in **Figure 1b** and **c** emphasize the Na(1) sites, with their neighboring Na(2) (orange spheres) and Si/P (red spheres) sites, resulting in distorted hexagonal prisms (silver). For visualization purposes, **Figure 1b** and **c** omit the Zr and O atoms.

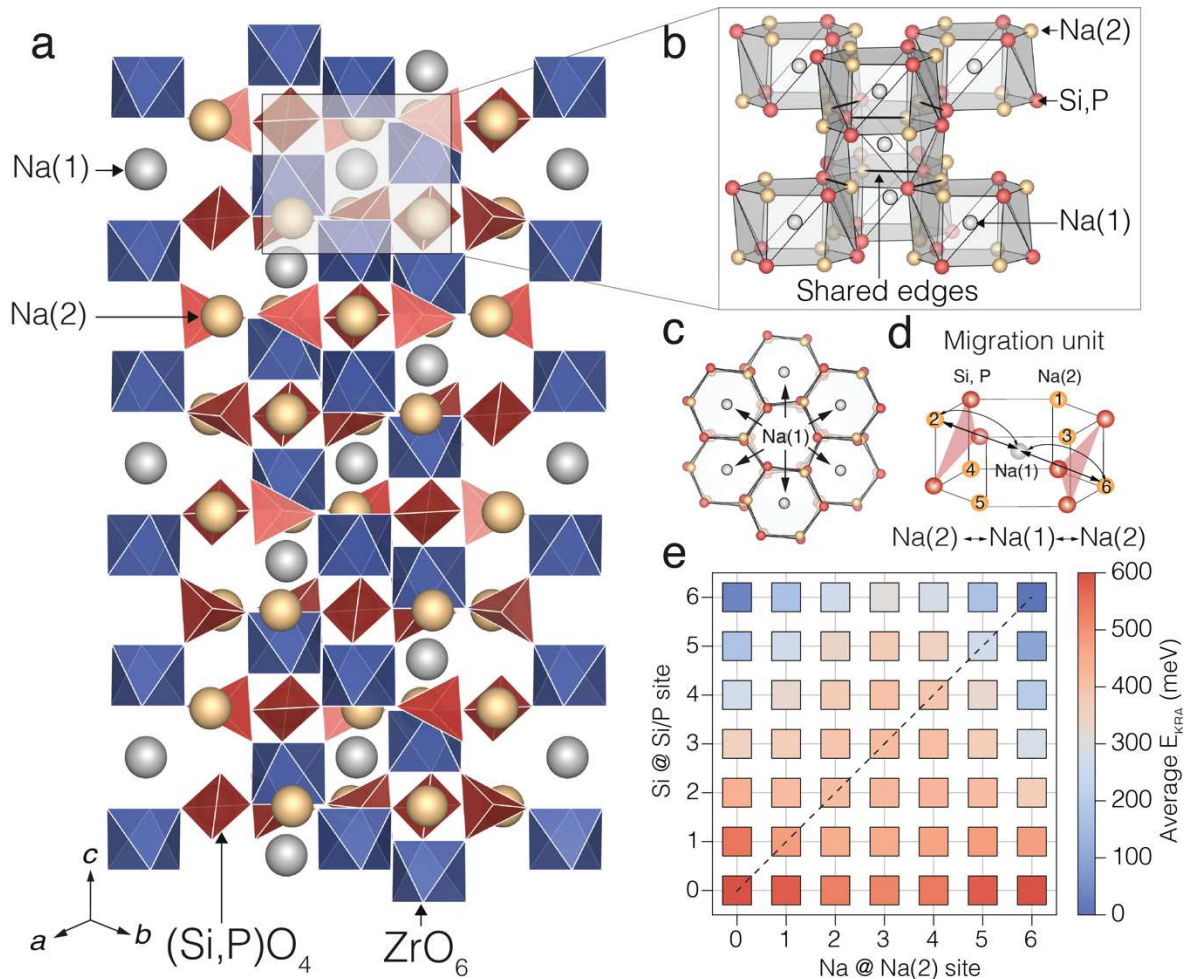


Figure 1 | Characteristics of sodium ion transport in NASICON. Structural models of $\text{Na}_{1+x}\text{Zr}_2\text{Si}_x\text{P}_{3-x}\text{O}_{12}$ (**a**, **b**, **c**, and **d**) and Na-migration barriers (**e**). In **a**, **b**, **c** and **d**, the Na(1) sites are indicated by silver spheres, the Na(2) by orange spheres, the (Si/P) O_4 groups by red tetrahedra, Si/P atoms by red spheres, and ZrO_6 units by blue octahedra. **b** and **c** depict the local environment of Na(1), with each Na(1) surrounded by six neighboring Na(2) atoms (orange spheres) and six Si/P (red spheres) atoms. For simplicity, O and Zr atoms are not shown in **b**, **c**, and **d**. Each silver hexagonal prism in **b** or **c** represents the first coordination shell of a Na(1) site. Panel **d** is the migration unit used to study Na-migration in NASICON, and Na must hop across several different migration units to ensure Na diffusion. Red triangles in **d** indicate the bottlenecks caused by Si/ PO_4 tetrahedra (oxygen atoms are not shown). **e** shows the averaged kinetically resolved activation (KRA) barriers for Na(2) \leftrightarrow Na(1) hops, with varying Na(2) site occupation and Si/P content per migration unit. The barriers were extracted from a local cluster expansion model, which was fitted to the calculated nudged elastic band (NEB) barriers. The diagonal line in **e** shows locally charge neutral Si/P configurations. The computed NEB barriers used for fitting to generate the heatmap in **e** are available in the supporting information (SI).

Figure 1d shows the smallest relevant unit –the migration unit– encompassing all possible migration events for Na-ions in NASICON. The migration unit centered around Na(1) highlights the connectivity between the Na(1) site and its closest six Na(2) neighbor sites, as well as the neighboring Si(P) atoms. Each migration unit (see **Figure 1b** and **c**) is edge-shared with six neighboring migration units, where each unit can exhibit its own distribution of Na/vacancies and Si/P. In the NASICON structure, Na-transport must always involve both Na(1) and Na(2) sites,^{18,30,33,34} giving rise to migration pathways of the kind Na(1) ↔ Na(2). The specific Na-migration pathway depends entirely on the Na and Si/P content within the structure,^{19,30,31} which sets the occupation and the relative stability of Na(1) and Na(2) sites. For example, at low Na content ($x = 0$), Na ions reside only in Na(1) sites, favoring a Na(1) ↔ Na(2) ↔ Na(1) pathway.^{17,30,32} At higher Na content ($x \geq 2$), both Na(1) and Na(2) sites are occupied to varying degrees (see later **Figure 2**), and any of the two migration pathways can be active.^{19,30} Importantly, for macroscopic Na diffusion to occur in NASICON, several successful migration hopping events, between adjacent migration units, need to happen, for which it is critical that Na atoms can hop from Na(1) to Na(2) sites (or vice-versa) within each unit. Thus, we considered a single migration event to be Na(1) ↔ Na(2) within a single migration unit, in the presence of varying Na and Si/P content.

For any Na composition in the range $0 \leq x \leq 3$, the concentrations of Si, and P are set by the NASICON stoichiometry, such that the composition guarantees global charge neutrality (i.e., the NASICON cell is electrostatically neutral). However, each migration unit can exhibit random occupancies of Si/P in Si/P sites, and Na/vacancies in the Na(2) sites (panels **b**, **c** and **d** of **Figure 1**). Consequently, the migration of Na-ions may occur through migration units that are not locally charge neutral, i.e., a given unit by itself may not be electrostatically neutral. In our work, we consider all possible

Na(1) \leftrightarrow Na(2) hopping events within a given migration unit, including scenarios with and without local charge neutrality.

We evaluated all the unique Na-ion migration pathways that are possible within a migration unit of **Figure 1d** using the nudged elastic band method (NEB)³⁵ together with density functional theory (DFT), and using the strongly constrained and appropriately normed (SCAN) meta-generalized gradient approximation.³⁶ The NEB method is designed to calculate migration barriers in solid electrolytes, as highlighted by prior studies.^{2,3,37,38} We identified 32 unique Na-hops, given the migration unit of **Figure 1d**, which included barriers computed at different Si and P compositions and Na/vacancy contents (**Section S2** of the Supporting Information, SI). The calculated migration barriers at 0 K are defined as the difference between the highest energy state and the configuration with the lowest energy—the initial and/or final end point.³⁷ The accuracy of our computed barriers is validated by the excellent agreement with existing data. For example, our calculated barrier at NaZr₂(PO₄)₃ (~ 458 meV, **Table S1**) agrees well with existing experimental values (~ 470 meV)²⁶ and *ab initio* MD (~ 472 meV).³²

Typically, migration events have an intrinsic directional dependence if the initial and final states are not equivalent, i.e., a Na(1) \rightarrow Na(2) hop may exhibit a different migration barrier compared to the reverse hop, Na(2) \rightarrow Na(1), due to energy differences between the end points, namely, Na(1) and Na(2). Van der Ven et al.³⁹ introduced the kinetically resolved activation (KRA) barrier, or E_{KRA} (see **Equation 2** in the **Methods** section) that removes the directional dependence of the migration barriers. Note that low values of E_{KRA} correspond to low values of migration barriers and vice versa. Furthermore, we trained a local cluster expansion (LCE) Hamiltonian⁴⁰ on the computed E_{KRA} values (listed in **Table S1** of the SI), which assigns a single

E_{KRA} value per migration unit and enables simulating large supercells of NASICON over long time-scales within our in-house kinetic Monte Carlo (kMC) package (**Methods** section and **Section S3** and **S4** of SI). The main advantage of the LCE over computationally expensive NEB calculations at all possible configurations, is that it enables the rapid estimation of E_{KRA} (and the corresponding migration barriers) at all Na(2), Si and P compositions in a given migration unit.

The average E_{KRA} values obtained by the LCE model are plotted in **Figure 1e**, with the dashed black diagonal indicating migration units that are locally charge neutral. Off-diagonal barriers are for locally charged situations and reflect multiple Na and Si/P configurations. For example, there are 400 possible configurations for a migration unit with 3 Na and 3 Si, and the E_{KRA} of ~ 410 meV (**Figure 1e**) is obtained by averaging the barriers across all the configurations. A similar averaging procedure is used for all scenarios where multiple Na/vacancy and Si/P configurations can exist within the same migration unit.

Depending on the Si/P environments, two distinct regions of high and low average E_{KRA} are inferred from **Figure 1e**. At lower Si or higher P content (bottom rows of **Figure 1e**), high average E_{KRA} (~ 500 meV or similar) are observed. In contrast, increasing the Si content or decreasing the P content (top rows of **Figure 1e**) lowers the average E_{KRA} (values as low as ~ 50 meV). Importantly, an increase in Si concentration in NASICON lowers the average E_{KRA} . The monotonic decrease in E_{KRA} (and migration barriers) with Si content can be attributed to lower $\text{Si}^{4+}\text{-Na}^+$ electrostatic repulsion compared to $\text{P}^{5+}\text{-Na}^+$ repulsion during Na-migration.

Changing the Na concentration at a given Si/P content within the migration unit does not result in a monotonic increase or decrease in average E_{KRA} . For instance, at

4/6 Si @ Si/P site in **Figure 1e**, the average E_{KRA} is low at both 0/6 Na @ Na(2) site and at 6/6 Na @ Na(2) site, with the average E_{KRA} reaching a maximum at 3/6 Na @ Na(2) site. This non-monotonic behavior is likely due to a combination of local electrostatic repulsions and local charge imbalance within the migration unit. For example, at 6/6 Na @ Na(2) site and 0/6 Si @ Si/P site (bottom right corner of **Figure 1e**), a high E_{KRA} can be attributed to the higher electrostatic repulsion between the Na^+ and P^{5+} ions. In contrast, low barriers at both 0/6 Na @ Na(2) and 6/6 Na @ Na(2) along 4/6 Si @ Si/P are likely because of high local charge imbalance that destabilizes the initial/final Na(1) and Na(2) configurations along the pathway. Eventually, high Na content in the migration unit contributes to low E_{KRA} , particularly at high Si content, as indicated by the blue squares towards the top right corner of **Figure 1e**. Indeed, the lowest values of E_{KRA} are observed at both high Na and high Si contents.

Combining the LCE and kMC, we investigated the relevant Na-transport properties in NASICON, such as ionic diffusivity and conductivity. The main advantage of using a kMC framework is the access to statistically significant amounts of data over large length and time scales, as well as the ability to sample a wide variety of configurations. By comparison, a classical or *ab initio* MD simulation^{3,23–25} performs a “one shot” representative calculation of a system at a given atomic configuration and composition, over smaller length and orders of magnitude shorter time scales.

In total, more than 2,000 kMC simulations were performed to predict the Na^+ diffusivities and conductivities at selected temperatures of 373, 473 and 573 K of 50 NASICON models (with varying Si/P configurations) at 11 distinct Na concentrations. Using canonical Monte Carlo simulations from our previous work,¹⁹ 550 starting NASICON configurations (50 configurations \times 11 concentrations) were generated at high temperature (~ 1500 K), which mimics the typical synthesis conditions and thermal

treatments of $\text{Na}_{1+x}\text{Zr}_2\text{Si}_x\text{P}_{3-x}\text{O}_{12}$ and other NASICON-based electrodes.^{17,28,30,41} Using high-temperature structures as starting configurations in our kMC guarantees a random distribution of PO_4 and SiO_4 tetrahedra in the NASICON structures, as observed in reports.^{17,30,32,41} The choice of temperatures for the study of Na-transport in our work (measured at 373 – 573 K) is largely motivated by the availability of experimental measurements to compare, but our framework can be easily extended to other temperatures as well. The comprehensive statistical analysis of this study, which addresses the role played by the PO_4 and SiO_4 distributions on overall Na-ion transport in $\text{Na}_{1+x}\text{Zr}_2\text{Si}_x\text{P}_{3-x}\text{O}_{12}$, is essential to capture differences occurring during the sample preparation.¹⁹

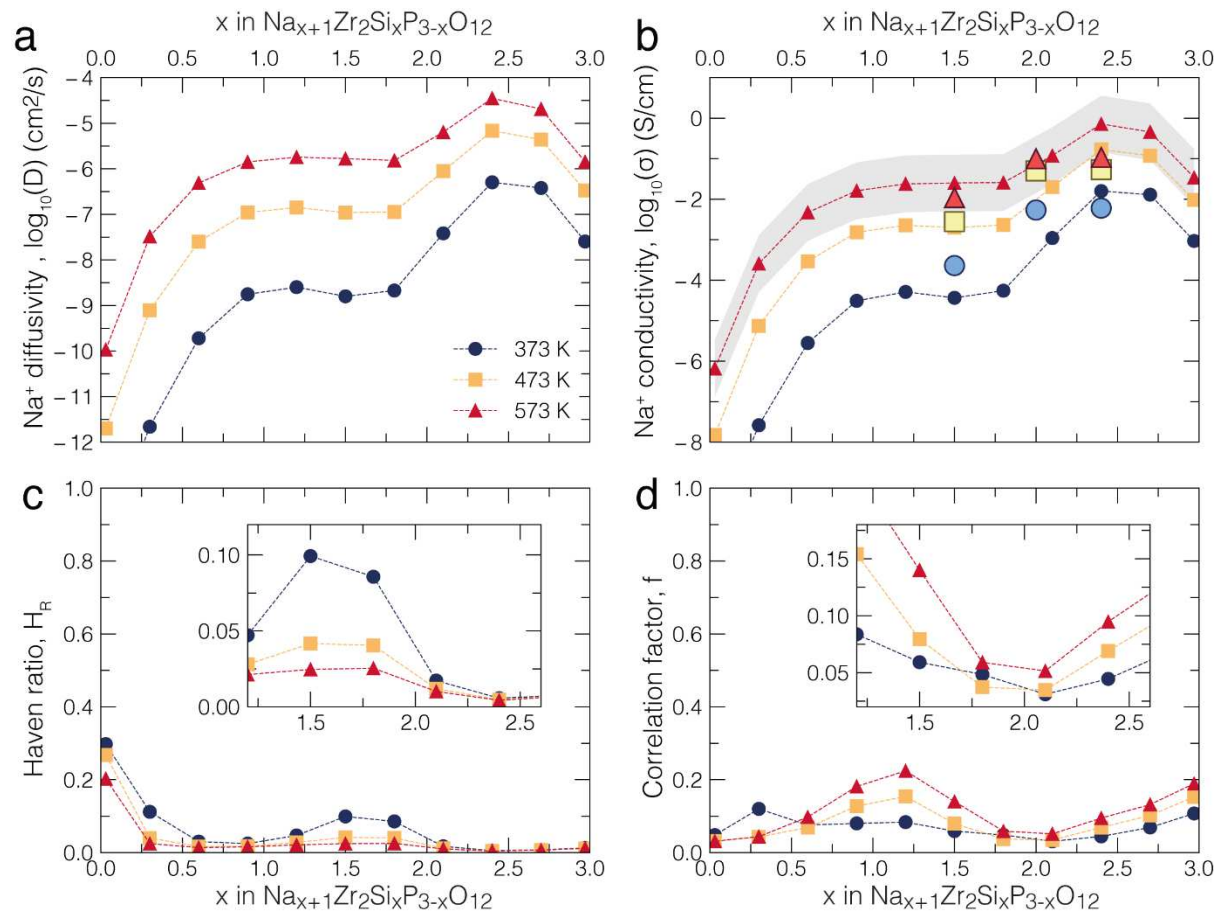


Figure 2 | Computed Na-ion transport properties of $\text{Na}_{1+x}\text{Zr}_2\text{Si}_x\text{P}_{3-x}\text{O}_{12}$ bulk based on kinetic Monte Carlo simulations. Calculated Na^+ diffusivity (**a**), conductivity (**b**), Haven's ratio (**c**) and averaged correlation factor (**d**) of $\text{Na}_{1+x}\text{Zr}_2\text{Si}_x\text{P}_{3-x}\text{O}_{12}$ at several temperatures: 373 (dark blue circles), 473 (orange squares) and 573 (red triangles) K, respectively. In panel **b**, the computed ionic conductivities are compared with the experimental values of this work (see **Figure 4** and **Figure S6** of the SI) at selected temperatures. Experimental values in **b** are depicted with larger light blue circles (373 K), yellow squares (473 K), and red triangles (573 K). An exhaustive comparison with previous experimental values of ionic conductivities is shown in the Supporting Information (**Figure S6**). The grey band in panel **b** shows the interval of confidence of our predictions at 573 K, which is lower in magnitude than the variance of Na-ion conductivities observed experimentally (**Figure S6**).

Figure 2 shows the computed Na^+ diffusivity (D , panel **a**), the conductivity (σ , panel **b**), Haven's ratio (H_R , panel **c**) and averaged correlation factor (f , panel **d**) at relevant temperatures of 373, 473, and 573 K, from kMC simulations of $\text{Na}_{1+x}\text{Zr}_2\text{Si}_x\text{P}_{3-x}\text{O}_{12}$ as the Na content (x) is varied. Note that the conductivity values (σ) in **Figure 2b** were calculated using the Nernst-Einstein equation, as expressed in terms of diffusivity D in **Equation 1**.^{3,23,24,39,40}

$$\sigma = \frac{e^2 C}{k_B T} D \quad (1)$$

where e is the elemental charge, C is the concentration of Na-ions, k_B is the Boltzmann constant and T is the temperature. Importantly, in **Equation 1**, D is the diffusivity of the center-of-mass of Na-ions in the NASICON structure, which includes cross-correlations of the migrations of different Na-ions (see **Section S4** of SI) and not the tracer diffusivity, as often used in many studies.^{23,39,40}

As confirmed by **Figure 2a** and **Figure 2b**, a temperature increase can significantly boost both Na⁺ diffusivities and conductivities across the full Na concentration. Interestingly, Na diffusivity and conductivity increase for increasing Na (and Si) concentrations up to $x \sim 2.4$, beyond which there is a drop in both diffusivity and conductivity. Thus, we conclude that Na-ion transport in Na_{1+x}Zr₂Si_xP_{3-x}O₁₂ is fastest at $x \sim 2.4$, at all temperatures considered in this work, which agrees with our experimental observations presented below.

Figure S6 reveals a significant spread of experimentally measured ionic conductivities from different reports,^{18,27,33,42–45} which is indicative of the difficulties in performing accurate measurements as well as the large variability in sample preparation. Nonetheless, for Na₃Zr₂Si₂P₁O₁₂ our measured experimental conductivity (see **Figure 4b**) of $\sim 0.1 \text{ S cm}^{-1}$ at 573 K is in excellent agreement with our computed value of $\sim 0.2 \text{ S cm}^{-1}$. Our model also agrees with previous measurements^{18,19,30,32} which report a low conductivity and diffusivity in Na₁Zr₂P₃O₁₂.

Previous studies have shown that correlated ion-migration can contribute to high diffusivity and conductivity in ionic conductors.^{3,4,7,23,32,40,46,47} In regimes of non-dilute diffusion carriers, the Haven's ratio (H_R) of **Figure 2c** quantifies the degree of cross-correlation between migrating Na⁺ ions, i.e., the extent to which individual Na⁺ hops contribute to the overall motion of the Na⁺ center-of-mass (**Equation S8** of SI). H_R varies between 1 (no cross-correlation or a random movement of individual Na⁺ ions) and 0 (fully correlated transport or non-random movement). While we observe small values of H_R (0.01 – 0.2) throughout the Na concentration range in the NASICON, indicating significant cross-correlation between Na ions, H_R at low Na concentrations ($x \sim 0$) is moderately high (~ 0.2) compared to high Na concentrations (H_R ~ 0.01 at $x \sim 3$). The variation in H_R with Na composition (x) can be partly attributed

to the occupancy of Na across the Na(1) and Na(2) sites in the NASICON. For example, at $x \sim 0$, Na^+ mostly resides in the Na(1) sites, which are separated from each other by large distances ($\sim 6.47 \text{ \AA}$), suggesting lower degrees of cross-correlations between migrating Na^+ ions. At $x \sim 3$, Na^+ ions populate both Na(1) and Na(2),³⁰ which are separated by shorter distances ($\sim 3.48 \text{ \AA}$) than Na(1)-Na(1), possibly facilitating correlated migration of Na^+ ions. Interestingly, cross-correlation between Na^+ ions shows an increase with increasing temperature, as indicated by the drop in H_R with rising temperature at all x (**Figure 2c**); this trend also coincides with increasing of D and σ , highlighting the positive impact of correlated motion on the overall Na-ion transport.

Another type of correlation, specifically between successive jumps of the same Na^+ ion, is to estimate the average correlation factor, f , of **Figure 2d** (see **Equation S10** of the **SI**). f measures the variation in local environments (resulting in a change of migration barriers) as experienced by individual Na^+ ions as they migrate through NASICON. f captures the deviation away from a truly random walk of a given Na^+ ion within the structure, with $f = 1$ indicating a true random walk and $f = 0$ signifying truly non-random walk. Thus, f is different from H_R , which describes the correlation between the motions of different Na^+ ions. Similarly, to our observations with H_R , we find that correlation effects, as measured by f , are quite pronounced at all Na concentrations in NASICON (**Figure 2d**). For example, f decreases progressively from 0.2 to 0.01 as x varies from 1 to 2. Notably, f exhibits more significant non-monotonic behavior compared to H_R in the range $0 < x < 3$.

One of the main reasons behind the high degree of correlation (as indicated by H_R and f) in NASICON is the high sensitivity of the E_{KRA^S} to the local Si/P environment (**Figure 1e**). Indeed, one may observe large variations in the local migration units,

which leads to significant changes in E_{KRA} , at a given Na concentration. This is clearly shown in **Figure S2**, where the migration barrier varies between ~ 300 meV and ~ 800 meV at $x \sim 2$. Every Na^+ migration event leads to a dynamic change in local environment by creating new vacancies and eliminating existing ones, which can have sizeable effects on the migration barriers (and hence E_{KRA}), eventually resulting in highly correlated motion.

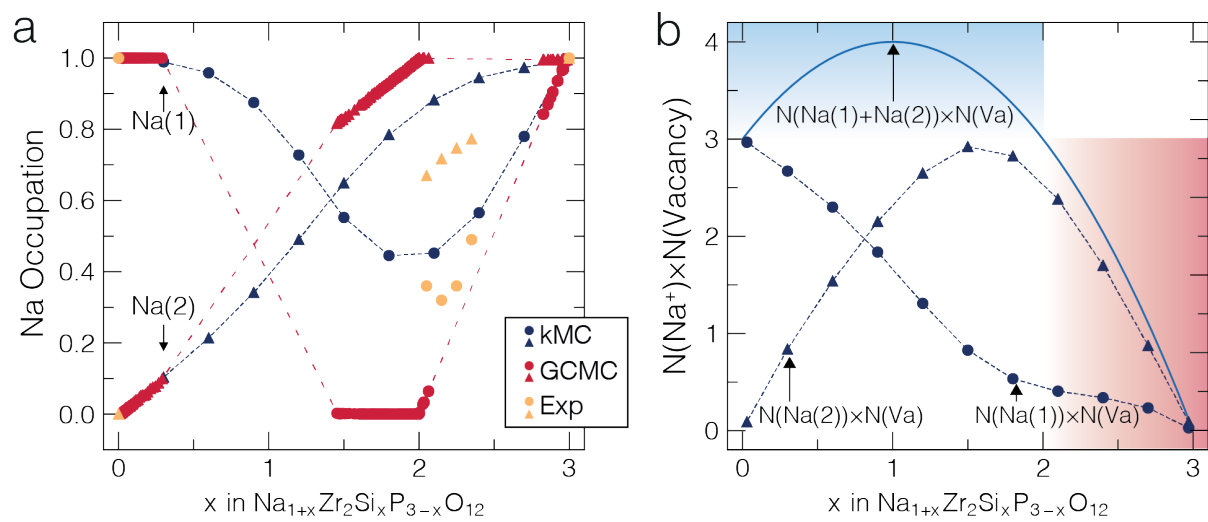


Figure 3 | Sodium occupancies and concentrations as a function of Na content. Panel **a** shows the averaged Na site occupancy at Na(1) site (blue circles) and Na(2) site (blue triangles) from kMC simulations at 443 K, and compared with previous Grand Canonical Monte Carlo simulations¹⁹ (red circles and triangles) at the same temperature, and existing experimental data³⁰ (in orange circle and triangles). Dashed lines are used as guide for the eye. Panel **b** shows $N(\text{Na}^+) \times N(\text{Vacancy})$ (solid blue curve, per f.u.) at 443 K from kMC simulations. The contributions to $N(\text{Na}^+) \times N(\text{Vacancy})$ from individual sodium sites, Na(1) and Na(2), are shown as blue dashed lines. In panel **b**, the shaded regions mark areas where Na^+ -ion conductivity is highly (red) or slightly (blue) impacted by the charge carrier concentration.

It is worth analyzing how the distribution of Na-ions, across the Na(1) and Na(2) sites controls the Na diffusivity (and conductivity) of NASICON. **Figure 3a** shows the

averaged Na occupancy of the Na(1) and Na(2) sites, as extracted from our kMC simulations. We compare these values with single-crystal X-ray diffraction experiments by Boilot *et al.*³⁰ at specific compositions, and our previous grand-canonical Monte Carlo simulations,¹⁹ which do not account for the dynamics of the Na⁺ ions.

In NASICONs,^{18,48} Na-transport can only occur if multiple exchanges between Na(2) \leftrightarrow Na(1) sites occur.^{18,30,31} This implies that both Na(1) and Na(2) must be occupied to some degree^{18,30,31} for facile transport. The Na site occupancies derived from our kMC data which includes possible Na-migration events, at 443 K (170 °C, blue shapes in **Figure 3a**) show that both Na(1) and Na(2) are partially occupied at compositions $1 < x < 3$. The kMC results are in qualitative agreement with X-ray measurements at 443 K of Ref. ³⁰ (orange shapes in **Figure 3a**). In contrast, occupations generated by the grand-canonical Monte Carlo model (red filled shapes in **Figure 3a**) indicate the equilibrium Na occupancies, which are distinctly different from the kMC simulations (and experiments) that include the impact of Na movement.

Importantly, both our kMC and grand-canonical Monte Carlo simulations indicate that at Na₁Zr₂P₃O₁₂, Na⁺ ions will be almost exclusively located at Na(1), even after including Na⁺ dynamics at 443 K (**Figure 3a**).³² In Na₁Zr₂P₃O₁₂, the Na(2) sites are empty because they are not thermodynamically stable at this composition.^{32,41} Thus, the lack of Na atoms present in Na(2) sites that can act as diffusion carriers, contributes significantly to the low D (and σ) observed at low Na content ($x \sim 0$, **Figure 2**), in addition to the high E_{KRA} observed (i.e., at low values of Na@ Na(2) and Si@ Si/P in **Figure 1e**).

By contrast, at high Na contents ($x \sim 3$, Na₄Zr₂Si₃O₁₂), Na⁺ diffusion is mostly limited by a lack of Na vacancies (either on Na(1) or Na(2) sites), which contributes to

the moderately low computed D and σ . Note that the computed E_{KRA} barriers achieve their lowest values corresponding to high Na and Si content (**Figure 1e**), which is similar to the local migration units that will be observed at $x \sim 3$, and should, in principle, contribute to increase D and σ . However, the sharp decrease in the number of available vacancies prevails over the decrease in E_{KRA} , eventually lowering D and σ . While we only consider vacancy-based migration mechanisms in our work, a recent study has also explored interstitial-based migration mechanisms in various solid electrolytes.⁴⁹ Given the robust agreement between our predictions and measurements, we believe that an interstitial-based mechanism is not active within NASICON structures.

Figure 3b further quantifies the extent of diffusion carrier availability within the NASICON structure. For example, the solid blue curve of **Figure 3b** shows the product of the number of Na ions and vacancies in the structure [$N(\text{Na}^+) \times N(\text{Vacancy})$], which is a proxy for the availability of diffusion carriers in the structure, as a function of Na content. **Figure 3b** also splits the concentration of Na ions, $N(\text{Na}^+)$, into site-specific quantities, $N(\text{Na}(1))$ and $N(\text{Na}(2))$, as indicated by the dashed blue curves.

In the blue-shaded region of **Figure 3b** in the range $0 < x < 2$, $N(\text{Na}^+) \times N(\text{Vacancy})$ is extended, signifying high availability of diffusion carriers, but the barriers for Na motion are large as well (bottom half of **Figure 1e**). In striking contrast, for $x > 2$, $N(\text{Na}^+) \times N(\text{Vacancy})$ decreases sharply, along with a decrease in E_{KRA} as well (top half of **Figure 1e**), signifying an increase in D and σ up to $x \sim 2.4$ followed by an eventual decline of both quantities as $x \rightarrow 3$. In **Figure 3a**, at $x = 3$, both Na(1) and Na(2) sites are filled and no free charge carriers are available.

Experimentally and theoretically,^{17–19,30} at $x \sim 2.4$ both Na(1) sites and Na(2) sites are expected to be occupied to some degree and the Na⁺ has enough vacancies to migrate. Furthermore, we expect the overall migration barriers to be low at $x \sim 2.4$ compared to $x < 2$, as quantified by trends in E_{KRA} in **Figure 1e**. Therefore, Na_{3.4}Zr₂Si_{2.4}P_{0.6}O₁₂ strikes the optimal combination of density of diffusion carriers (i.e., availability of Na ions and vacancies in both Na(1) and Na(2) sites), and low migration barriers to achieve the fastest Na-transport in the NASICON electrolyte.

We have synthesized different compositions of the NASICON, namely, Na_{2.5}Zr₂Si_{1.5}P_{1.5}O₁₂, Na₃Zr₂Si₂P₁O₁₂, and Na_{3.4}Zr₂Si_{2.4}P_{0.6}O₁₂ and tested their Na-ion transport characteristics. **Figure 4a** shows the powder X-ray diffractions (PXRD) measured at room temperature, with the PXRD profiles matching the rhombohedral ($R\bar{3}c$) Na_{2.5}Zr₂Si_{1.5}P_{1.5}O₁₂, the monoclinic ($C2/c$) Na₃Zr₂Si₂P₁O₁₂, and $C2/c$ - Na_{3.4}Zr₂Si_{2.4}P_{0.6}O₁₂ structures, respectively. Information about the synthesis of these NASICON compositions are discussed in the **Methods** section.

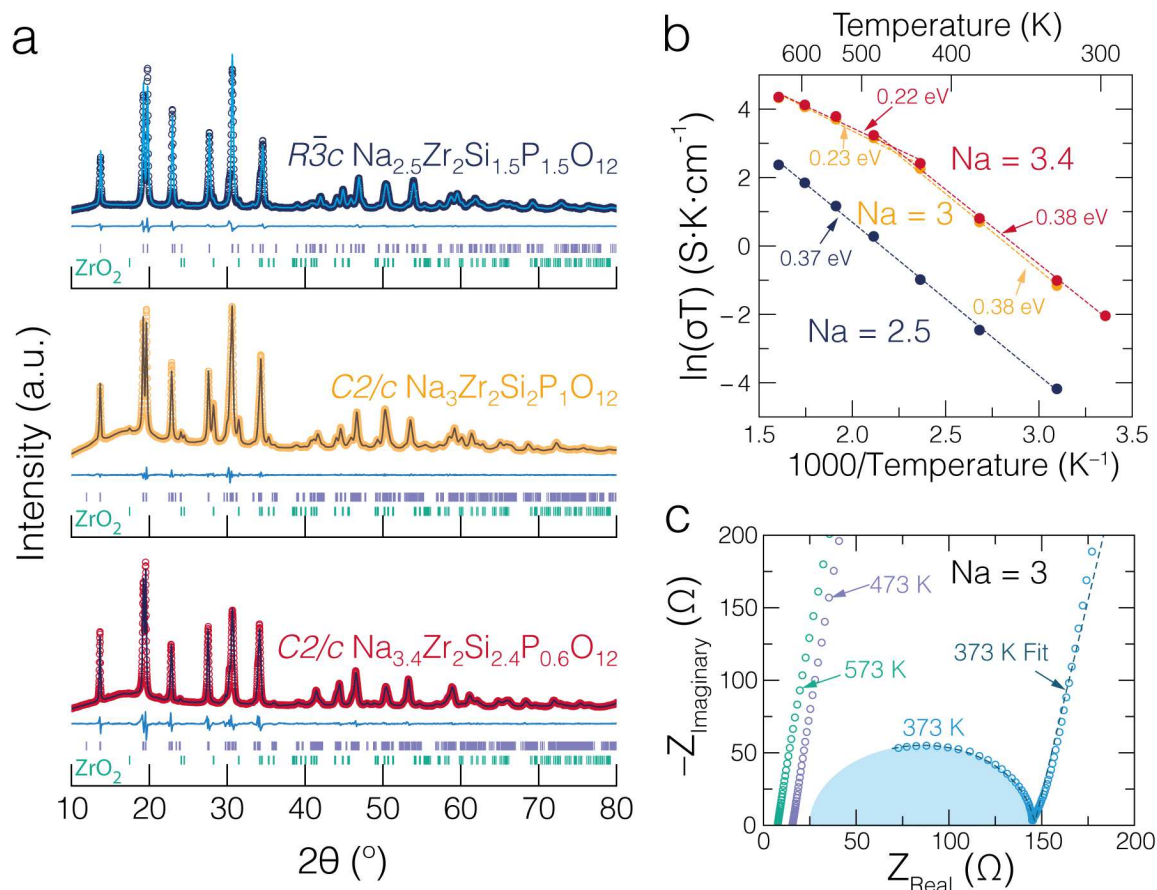


Figure 4 | Room temperature powder X-ray diffraction of selected NASICON compounds and their ionic conductivities measured using the pellets formed by these powders. In panel **a**, X-Ray diffraction pattern (dark blue, orange, and red circles), and Le Bail fitting (solid lines in cyan, dark brown and dark red) for synthesized $\text{Na}_{1+x}\text{Zr}_2\text{Si}_x\text{P}_{3-x}\text{O}_{12}$ ($x = 1.5, 2.0,$ and 2.4). **b** Arrhenius plot from AC impedance measurements of synthesized samples ($x = 1.5$ in dark blue, $x = 2.0$ in orange, $x = 2.4$ in red). **c** Representative Nyquist plot for $\text{Na}_3\text{Zr}_2\text{Si}_2\text{P}_1\text{O}_{12}$ at variable measured at 373 (blue), 473 (purple) and 573 K (green). Other Nyquist plots are **Figure S9** in the SI.

The refined lattice parameters of $\text{Na}_{2.5}\text{Zr}_2\text{Si}_{1.5}\text{P}_{1.5}\text{O}_{12}$, $\text{Na}_3\text{Zr}_2\text{Si}_2\text{P}_1\text{O}_{12}$ and $\text{Na}_{3.4}\text{Zr}_2\text{Si}_{2.4}\text{P}_{0.6}\text{O}_{12}$ are listed in **Table 1** and are in agreement with existing reports.^{17,50} The phase purity of these compounds enables us to characterize their variable temperature Na ionic conductivities, as reported in the Arrhenius plots of **Figure 4b**.

Impedance spectra at variable temperatures and their fitting details are also provided in **Figure S9** and related text in the SI.

Table 1 | Lattice parameters of selected NASICON samples obtained from room temperature PXRD. Lattice constants, angles and volumes are in Å, °, and Å³, respectively. Z is the number of formula units.

	Na _{2.5} Zr ₂ Si _{1.5} P _{1.5} O ₁₂	Na ₃ Zr ₂ Si ₂ P ₁ O ₁₂	Na _{3.4} Zr ₂ Si _{2.4} P _{0.6} O ₁₂
Space group	<i>R</i> $\bar{3}$ <i>c</i>	<i>C</i> 2/ <i>c</i>	<i>C</i> 2/ <i>c</i>
<i>a</i>	8.9864(13)	15.6565(16)	15.7571(15)
<i>b</i>	8.9864(13)	9.0634(7)	9.0835(7)
<i>c</i>	22.960(5)	9.2216(15)	9.2549(8)
β	–	124.255(8)	124.963(5)
Volume	1605.7(5)	1081.6(2)	1085.58(16)
Z	6	4	4
Volume/Z	267.6	270.4	271.40

The ionic conductivities of the synthesized Na_{1+x}Zr₂Si_xP_{3-x}O₁₂ phases at variable temperature were fitted with appropriate equivalent circuits (see **Methods** section). The extracted activation energies for all three NASICON compositions were obtained from the Arrhenius plots (ln(σ T) vs. 1000/T) of **Figure 4b**. For the composition x = 1.5, the extracted activation energy is ~ 0.37 eV, and no phase transition is observed due to the stability of the rhombohedral phase at room and higher temperatures. Both compositions at x = 2.0 and x = 2.4 show two linear domains with different activation energies displayed in **Figure 4b**. Thus, the Arrhenius plots of **Figure 4b** reproduce the documented monoclinic-to-rhombohedral phase transition upon heating for the compositions Na₃Zr₂Si₂P₁O₁₂, and Na_{3.4}Zr₂Si_{2.4}P_{0.6}O₁₂ at ~ 433 ± 15 K.^{51–53} Heating and cooling responses of ionic conductivity vs. temperature for the three compositions are discussed in **Figure S10** of the SI. The activation energies for x = 2.0 are 0.38 eV (below the phase transition ~ 433 K) and 0.22 eV (above ~ 433 K), which are in good agreement with previous works.^{41,54–60} Na_{3.4}Zr₂Si_{2.4}P_{0.6}O₁₂ shows similar activation

energies, with values of 0.38 eV (below ~ 433 K) and 0.22 eV (above ~ 433 K) at $x = 2.4$, in agreement with Ref. ⁵⁴.

An example of a Nyquist plot used to extract the total ionic conductivity from the sintered pellets of the NASICON compositions at variable temperatures (373 K, 473 K, and 573 K) is given in **Figure 4c**. The composition with $x = 1.5$ has the lowest ionic conductivity for all temperatures compared to structures with $x = 2.0$ and 2.4. Note, low-temperature impedance measurements of the monoclinic $\text{Na}_{3.4}\text{Zr}_2\text{Si}_{2.4}\text{P}_{0.6}\text{O}_{12}$ phase do indicate high Na-conductivity.⁵⁸ The ionic conductivity of $x = 2.0$ showed that the measured values of this work are within the range of reported values.^{41,61,43,44,18,45,27}

Discussion

Experimentally, ionic diffusivity can be measured by a number of techniques, such as solid-state nuclear magnetic resonance, quasi elastic neutron scattering and secondary-ion mass spectroscopy,^{20,62} while AC impedance spectroscopy is the method of choice for determining ionic conductivity in solid electrolytes.⁶³ Indeed, we have used AC impedance spectroscopy in this study. Although classical and *ab initio* molecular dynamics simulations have proved invaluable in the prediction of ionic conductivities in solid electrolytes,^{2,3,7,20,22,24,40,46,64–67} we have demonstrated that first-principles-based kMC can access significantly longer time scales in the millisecond range and larger length scales (a total of 21,504 atom supercells in the present work), enabling us to approach experimental time and space resolutions and establish a robust link between measurements and theory. To the best of our knowledge, this is

the first study to use a LCE+kMC approach, bearing the accuracy of DFT calculations, to probe the ion-dynamics in solid electrolytes.

Our kMC simulations provide the hopping frequencies of Na⁺ migration, of different Na concentrations and temperatures, which can be efficiently evaluated and mapped in large supercell models. The hopping frequency is defined in **Equation S4** in the SI and includes the attempt frequency and the migration barrier. From our kMC data, we plot heatmaps indicating the spatial migration of Na-ions in **Figure 5**, along with the frequency associated with each Na migration event. **Figure 5** shows the hopping frequency of three representative NASICON compositions, i.e., $x = 0.3$, 2.4, and 2.97, capturing Na-ion transport in low, intermediate, and high sodium concentrations. Each panel in **Figure 5** contains 1,024 migration units (**Figure 1e**), where each migration unit is represented by a distinct colored hexagonal prism. In **Figure 5**, the migration units with high hopping frequencies, shown by red prisms, imply that Na-ions have a high probability of migrating beyond the migration unit, thus contributing actively to macroscopic diffusion (the inference is vice versa for blue/purple prisms corresponding to low hopping frequencies). Expectedly, as discussed in **Figure 2**, $x = 2.4$ shows significantly higher hopping frequency compared to compositions $x = 0.3$, and 2.97.

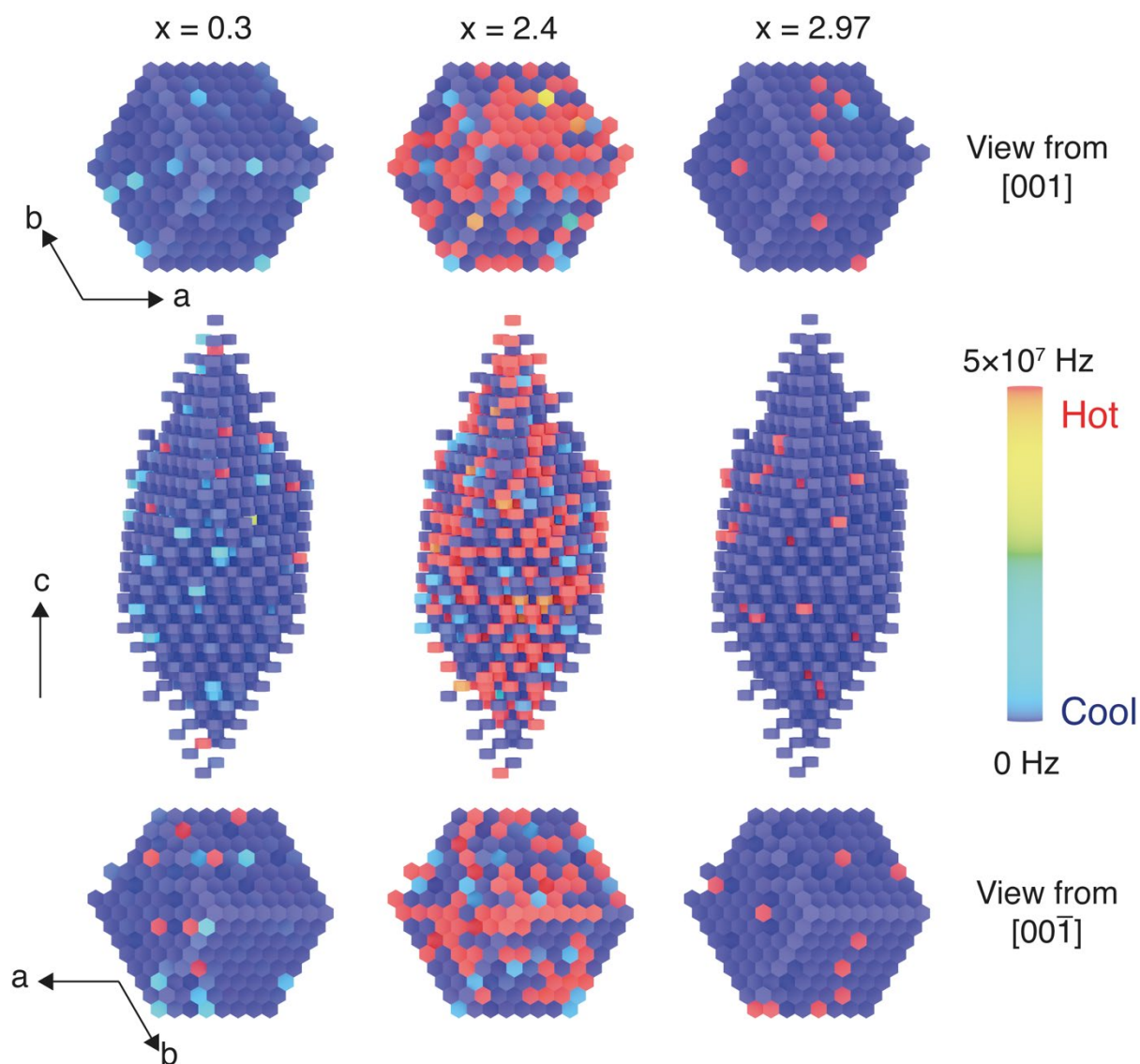


Figure 5 | Sodium hopping frequencies in NASICON materials. Heatmap representation of the frequency (in Hz) of Na-ion migration from selected kMC simulation supercells ($8 \times 8 \times 8$ of the primitive cell, including 1,024 migration units) at Na contents of $x = 0.3$, 2.4 and 2.97 . The temperature in all panels is 573 K. Each colored hexagonal prism represents a migration unit, as exemplified in **Figure 1d**. The hopping frequency of each migration unit is taken by averaging the probability of the six possible migrations of Na^+ between the central Na(1) site and the six Na(2) sites in each unit. The top and bottom panels show views along the c -axis from above and below the supercells.

The direct visualization of the hopping frequency of Na^+ migration is insightful for unravelling the respective effects played by PO_4 and SiO_4 moieties on the overall Na^+ transport. In **Figure 5**, at low Na concentrations, e.g., $x = 0.3$, most migration units

appear purple (low frequency) signifying low diffusivity/conductivity, whereas these blue regions turn progressively to yellow and eventually red for increasing values of x . At $x \sim 2$, most Na-ions are actively engaged in ion transport as most migration units are red (**Figure 5**), highlighting facile ionic transport, consistent with the highest values of observed D and σ at $x \sim 2.4$ (**Figure 2**). As x approaches 3 ($x \sim 2.97$ shown in **Figure 5**), the color of the migration units eventually become purple, coinciding with the drop in D/σ at high Na-contents (**Figure 2**) due to the low availability of Na-vacancies. This informative analysis can be extended to other topical solid electrolytes with mixed polyanion sulfides, such as, GeS_4 , PS_4 , SiS_4 , etc.^{8,9,12-14}

The underlying structural models to generate the data in **Figure 5** are based on disordered NASICON structures, where at a given Na concentration the SiO_4 and PO_4 units are randomly distributed. This is also the case of the most researched sulfide electrolytes for Li-ion solid-state batteries with various degree of mixing of GeS_4 , SiS_4 , SiS_4 and SnS_4 moieties.^{9,11-14} Thus, these NASICON structures truly mimic the experimental synthesis conditions (~ 1200 °C for solid-state synthesis^{18,33}) and/or heat treatments (e.g., low-temperature sol-gel synthesis^{27,68} followed by sintering at ~ 1200 °C for densification^{18,33,68}), which quench the disorder of the phosphate and silicate units accessed at high temperatures. Previously we have shown that under equilibrium conditions NASICON should phase separate into P-rich and Si-rich domains, particularly across Na concentrations from $x = 0$ to 2.¹⁹ It is also important to understand the impact of phase separation (or lack thereof) on Na-diffusivity and conductivity.

We have extended our kMC model to structures produced in regimes of complete phase separation in **Figure S7** of the SI. Notably, the computed ionic conductivity and other related quantities predicted in regimes of phase separation look

similar to those reported in **Figure 2**, with the exception of a dip in D and σ around $x \sim 1.8 - 2$ compared to the scenario of fully disordered system (non-phase separated). However, this dip in ion transport properties approximately accounts for one order of magnitude, well within the error of the available experiments and our calculations, thus making it challenging to detect the signature of phase separation via diffusivity/conductivity measurements or calculations. Our calculations suggest that Na diffusivity and conductivity cannot be used to identify the underlying phases within the NASICON electrolyte. We believe this conclusion may also be valid for other solid electrolytes and electrodes of interest, particularly those adopting the NASICON structure, which can also thermodynamically favor phase separation.^{69,70} Notably, heatmaps produced in structures with phase separation (**Figure S8**) do clearly depict the presence of phase boundaries (differentiating Si-rich and P-rich domains), indicating that robust structural characterizations are still the best way of detecting phase separation.

Our computed barriers and kMC simulations suggest that higher Na^+ conductivity in NASICON can simply be achieved by increasing the SiO_4 to PO_4 ratio. There are two reasons for this: (i) higher Si^{4+} content decreases that of P^{5+} cations in the system, thereby reducing the electrostatic repulsion between the Na^+ and P^{5+} cations during Na migration, and (ii) due to the longer Si-O bonds in SiO_4 compared to the P-O bonds in PO_4 , Si-rich migration units will be larger, facilitating migration of large ions, such as Na^+ . Thus, tuning the Si concentration (or, equivalently, increasing the number of 4+ instead of 5+ cations within the polyanion groups) in the NASICON structure (via aliovalent doping, for example), clearly provides a new way for optimizing ionic transport in this class of ionic conductors.

Indeed, the last ~40 years of research on NASICON materials has investigated aliovalent doping as a way to improve the Na-ion conductivity of this material. An increase of Na ions is typically achieved by subvalent doping of the Zr^{4+} with trivalent Al^{3+} , Cr^{3+} , Dy^{3+} , Er^{3+} , Fe^{3+} , Gd^{3+} , In^{3+} , Sc^{3+} , Tb^{3+} , Y^{3+} and Yb^{3+} , and/or divalent Co^{2+} , Mg^{2+} , Ni^{2+} and Zn^{2+} species.^{32,26,28,71–73,41} Combining a high Si content in the structure with trivalent doping on Zr^{4+} can potentially improve Na transport at high Na concentrations in NASICONs ($x \rightarrow 3$). Alternatively, supervalent doping on the Zr^{4+} site with V^{5+} , Bi^{5+} , Sb^{5+} , Nb^{5+} and Ta^{5+} cations is used to increase the number of Na vacancies, and also to reduce (by ~ 30 K) the temperature of the monoclinic-to-rhombohedral phase transition.⁷⁴ Supervalent doping is also a viable strategy for increasing the Si content in the NASICON structure while preserving the stoichiometric ratio of Na-ions and vacancies. Specifically, the ionic radii of Sb^{5+} (~ 0.60 Å), Nb^{5+} (~ 0.64 Å) and Ta^{5+} (~ 0.64 Å) in octahedral environments appear compatible with that of Zr^{4+} (~ 0.72 Å).⁷⁵ The higher stability of the 5+ oxidation state of the three candidates represents the most viable choice for incorporating more Si into the NASICON structure. Furthermore, it has been shown that isovalent doping of Ge^{4+} on Si^{4+} can also increase the size of the migration unit,⁷⁶ potentially facilitating Na-diffusion.

Conclusions

We have used a combination of state-of-the-art computational tools to explain the influence of polyanion mixing, composition and temperature on ionic transport in $\text{Na}_{1+x}\text{Zr}_2\text{Si}_x\text{P}_{3-x}\text{O}_{12}$, as an example ionic conductor. This was achieved by using a combination of density functional theory-based nudged elastic band calculations, a local cluster expansion Hamiltonian, and kinetic Monte Carlo simulations over millisecond timescales and nanometer length scales. Our study has demonstrated that low migration barriers for Na^+ -ions can be achieved by having local environments that are rich in Si and Na, which can be attributed to the lower electrostatic repulsion between Si^{4+} and Na^+ (vs. P^{5+} and Na^+) during Na migration. A further increase of Si content in $\text{Na}_{1+x}\text{Zr}_2\text{Si}_x\text{P}_{3-x}\text{O}_{12}$ can be achieved by doping Zr with stable 5+ cations, such as Ta, Nb, Sb, while maintaining an optimal Na composition. Importantly, we discovered a complex interplay between migration barriers and diffusion carrier availability in determining the overall ionic diffusivity/conductivity. For example, at low Na concentrations ($0 < x < 2$), high migration barriers dominate, resulting in a gradual increase in diffusivity/conductivity with increasing x . At high Na concentrations ($x > 2.5$), the lack of diffusion carriers dominates (despite low migration barriers), resulting in a drop in diffusivity/conductivity. Thus, we observe that a Na composition of $x \sim 2.4$ is optimal in terms of combining enough diffusion carriers with low migration barriers, resulting in the highest diffusivity/conductivity. Through synthesis and characterization of the $\text{Na}_{3.4}\text{Zr}_2\text{Si}_{2.4}\text{P}_{0.6}\text{O}_{12}$, we have confirmed its high Na-conductivity, as predicted by our simulations. Using $\text{Na}_{1+x}\text{Zr}_2\text{Si}_x\text{P}_{3-x}\text{O}_{12}$ as a model system, we demonstrated the importance of sampling statistically vast composition, length, and time scales to capture the highly correlated ionic motion that can be observed in mixed polyanion systems. Our findings are significant for the optimization of mixed polyanion solid

electrolytes, such as sulfide-based systems which can achieve regimes of super-ionic conductivity.

Methods

Sodium Migration Barriers from Density Functional Theory

Na migration barriers were calculated using the nudged elastic band (NEB) method³⁵ through density functional theory (DFT) simulations as implemented in the Vienna ab initio simulation package (VASP).^{77,78} All the calculation parameters used in the DFT simulations can be found in **Section S2** of the SI. The NEB barriers were modeled at 3 representative Na concentrations, at $x = 0, 2,$ and 3 as in $\text{Na}_{1+x}\text{Zr}_2\text{Si}_x\text{P}_{3-x}\text{O}_{12}$. This selection is motivated by our previous knowledge on the compositional phase diagram of $\text{Na}_{1+x}\text{Zr}_2\text{Si}_x\text{P}_{3-x}\text{O}_{12}$,¹⁹ where NASICON exhibits three distinct ground states at 0 K.

Special care is required for the NEB barrier calculations of $\text{NaZr}_2(\text{PO}_4)_3$ ($x = 0$) which follows a pathway $\text{Na}(1) \rightarrow \text{Na}(2) \rightarrow \text{Na}(1)$. In $\text{NaZr}_2(\text{PO}_4)_3$ all the $\text{Na}(1)$ sites are occupied and Na migration is only possible if vacancies in $\text{Na}(1)$ are introduced. For this specific case the energy required for Na^+ migration should also include the formation energy of Na vacancy, which we computed using the method of Ref. ⁷⁹. We found that the Na vacancy formation energy in $\text{NaZr}_2(\text{PO}_4)_3$ is ~ 474 meV, which we added in our model (see SI). Whereas the Na vacancy formation energy at $x = 2$ and 3 is negligible (~ 13 meV). Note that at $x = 2$, $\text{Na}(1)$ and $\text{Na}(2)$ are only partially occupied which guarantees facile Na transport.

To remove the directional dependence of migration barriers, we define the kinetically resolved activation (KRA) barrier, E_{KRA} of **Equation 2**,

$$E_{KRA} = E_{\text{barrier}}[\text{Na}(1) \leftrightarrow \text{Na}(2)] - \frac{1}{2}(\Delta E_{\text{end}}) \quad (2)$$

where the $E_{\text{barrier}}[\text{Na}(1) \leftrightarrow \text{Na}(2)]$ is the NEB barrier,^{39,40} and ΔE_{end} is the absolute difference between the computed energies of the initial and final end point structures. The distribution of E_{KRA} at different configurations of Na and Si/P environments is shown in **Figure S1**, **S2**, **S3**, and **Table S1** of the SI.

Local Cluster Expansion Hamiltonian

The calculated E_{KRA} are fitted to a local cluster expansion (LCE) Hamiltonian built around a migration unit (see **Figure 1d**) centered on the Na(1) site and using a cut-off radius of 5 Å. Details of the LCE model and the fitting strategy are given in the SI. The fitted Hamiltonian can be used efficiently to compute migration barriers inside the migration unit at any given Na/vacancy and Si/P content/configuration. The LCE Hamiltonian includes 1 point, 5 pair, and 1 triplet terms (see **Table S3** and **Table S4**), respectively. The LCE Hamiltonian can reproduce the migration barriers with a RMS error of $\sim \pm 38$ meV. The robustness of the LCE Hamiltonian was cross-validated using the leave-one out method. Notably, a variability of $\sim \pm 38$ meV corresponds to a less than an order of magnitude in diffusivity (± 60 meV),⁸⁰ which is the typical uncertainty of experimental measurements and theoretical calculations for electrode materials.⁴⁰

Kinetic Monte Carlo Simulations

We implemented a rejection-free kinetic Monte Carlo (kMC) simulation scheme in an in-house-code, as described in Refs.^{39,40}. The initial configurations for the kMC were

generated using the canonical Monte Carlo simulation (based on our previous work where we constructed a global cluster expansion model on the NASICON)¹⁹ in an 8×8×8 supercell at $0 \leq x \leq 3$ containing 4,096 distinct Na sites and 3,072 Si/P sites. These structures were generated at 1500 K, and close to the experimental synthesis temperature.^{17,34,28,41} For each of the 11 compositions sampled ($x = 0.03, 0.3, 0.6, 0.9, 1.2, 1.5, 1.8, 2.1, 2.4, 2.7, 2.97$), 50 structural models were generated using the canonical Monte Carlo approach.¹⁹

We used kMC to evaluate the transport properties of NASICON crystals, including Na⁺ diffusivity, bulk conductivity, Haven's ratio, and correlation factor. These physical quantities are averaged for each of the 50 initial configurations per Na composition. During the kMC simulation, only Na ions can hop while the remaining atoms are frozen. Each kMC simulation included 2,048,000 equilibration steps, followed by 12,288,000 sampling steps for statistical analysis at 373, 473 and 573 K, respectively. In total, we have run 1650 independent kMC simulations (11 compositions×50 initial configurations ×3 temperatures) with a total of ~14 million steps per configuration, which totals to approximately 23 billion kMC steps. For investigating the impact of phase separation on ionic transport, we followed the same procedure as above, except the canonical Monte Carlo, equilibrated structures were generated at 573 K, instead of at 1500 K.

Synthesis and X-ray Characterization of Na_{1+x}Zr₂Si_xP_{3-x}O₁₂ Compositions

Synthesis of Na_{1+x}Zr₂Si_xP_{3-x}O₁₂ for $x = 1.5$ and $x = 2.0$ were carried out using a sol-gel method with NaNO₃, NH₄H₂PO₄, ZrO(NO₃)₂.xH₂O, Si(OC₂H₅)₄ (Tetraethyl orthosilicate/TEOS) and citric acid as precursors followed by carefully optimized

thermal treatments. Citric acid was first mixed with 300 mL of ethanol:deionized water (1:1), at 343 K for 1 hour. Then a stoichiometric amount of the precursors was introduced to the solution and the temperature was raised to 363 K for 1.5 hours. The resulting gel was then dried for 8 hours, at 453 K. A first calcination was carried out at 873 K for 8 hours, followed by second calcination at 1373 K for 18 hours. For the composition $x = 2.4$, a solvent-assisted solid-state reaction method was applied.⁵⁴ Corresponding amounts of NaNO_3 , and $\text{ZrO}(\text{NO}_3)_2$ were dissolved into deionized water. A stoichiometric amount of $\text{Si}(\text{OC}_2\text{H}_5)_4$ was also added to the solution while stirring. When $\text{Si}(\text{OC}_2\text{H}_5)_4$ was hydrolyzed, the corresponding amount of $\text{NH}_4\text{H}_2\text{PO}_4$ was added to the system while stirring. The homogeneous aqueous system then changed to a mixture of a colloidal sol and precipitates of complex zirconium oxyphosphate compounds. The whole mixture was dried at $\sim 85^\circ\text{C}$. The dried powder was calcined at $\sim 800^\circ\text{C}$ for 3 hours. After calcination, a white powder was obtained. The calcined powder was then milled in ethanol with zirconia balls on a milling bench for 48 hours and dried at $\sim 70^\circ\text{C}$ for 12 hours. The as-prepared powder (which was just calcinated at 1073 K) was then sintered at $\sim 1373\text{ K}$ for 18 hours to crystallize the phase.

X-Ray diffraction patterns of the obtained white powders were then measured at room temperature using a Bruker D8 diffractometer with copper source, ($K_{\alpha 1}=1.54056\text{ \AA}$ and $K_{\alpha 2}=1.54439\text{ \AA}$), and a step size of 0.021° . Profile matchings were done using WinPLOTR and FullProf software.⁴¹ For $x = 1.5$ the pattern was fitted using the $R\bar{3}c$ space group,^{18,76,81,82} while $x = 2.0$ and $x = 2.4$ were fitted using the $C2/c$ space group.^{41,83}

Variable temperature impedance measurements of $\text{Na}_{1+x}\text{Zr}_2\text{Si}_x\text{P}_{3-x}\text{O}_{12}$

For the preparation of impedance measurements, the three samples were cold pressed into 6 mm pellets and sintered at ~ 1373 K for 12 hours. The sintered pellets were then gold-sputtered (~ 75 nm), and carbon paper (papyex) was added on each side of the pellet to ensure good contacts for the impedance measurements in the high temperature impedance cell BioLogic HTSH-100. The latter was inserted in high temperature furnace BioLogic HTF-1100 and connected to impedance analyzer BioLogic MTZ-35 with a two-point connection. The frequency range used was from 0.1 Hz to 30 MHz, with an amplitude of 0.02 V. Measurements were recorded every 50 K from 323 K to 623 K (15 minutes soaking each time), and then cooled down every 50 K from 623 K to 323 K.

The fitting of Nyquist plot was carried out using ZView software. For $x = 1.5$, the equivalent circuit used was based on semicircle phenomena as seen in other reports,^{28,59,84–86} with R1 representing the contact resistance, parallel of CPE1 and R2 representing the semi-circle, and initially a CPE2 for the diffusion tail. Since CPE2 has an n -value close to 0.5, a Warburg element is used to better fit the diffusion tail. Applying the same equivalent circuit for other samples ($x = 2.0$ and $x = 2.4$) was not satisfactory, thus a one-phenomena Debye Model for solid electrolyte between two ionically blocking electrodes is used instead.⁸⁷ Schematics of the equivalent circuits are shown in **Figure S9** of SI.

Acknowledgments

P.C., C.M., A.K.C., E.M., V.S., and J.-N. C. are grateful to the ANR-NRF for the funding of the NRF2019-NRF-ANR073 Na-MASTER project. P.C. and Z.D. acknowledge funding from the National Research Foundation under NRF Fellowship NRFF12-2020-

0012. T. P. M. was supported by the National Research Foundation (NRF) Singapore through Singapore MIT Alliance for Research and Technology (SMART)'s Low Energy Electronic Systems (LEES) IRG. The computational work was performed on resources of the National Supercomputing Centre, Singapore (<https://www.nscg.sg>). We thank Dr. Theodosios Famprakis at TUDelft for fruitful discussion.

Authors Contributions

P.C. designed and supervised the project. Z.D., T.P.M., and P.C. performed the NEB simulations and fitted the local cluster expansion Hamiltonian with discussions with G.S.G. Z.D. developed all the tools for constructing models, Hamiltonian fitting, kinetic Monte Carlo and data analysis. Q.M. and E.M. carried out the synthesis of the NASICON phases, E.M. performed the PXRD, and the impedance measurements. E.M. performed the data analysis of the experimental data under the supervision of J.-N. C., V.S. and C. M. Z.D., T.P.M. and P.C. wrote the first draft. Z.D., P.C., G.S.G. and A.K.C. contributed to the initial data analysis of the computed data. All the authors contributed to the discussion and final version of this manuscript.

Conflicts of Interests

There are no conflicts to declare.

Supplementary information

The supplementary Information contains details of the density functional theory simulations, nudged elastic band results, kinetic Monte Carlo simulations, AC impedance measurements, equivalent circuits for the analysis of the AC-impedance

data, and the Arrhenius plot of conductivities vs 1/temperatures of selected NASICON compositions.

Code and Data Availability

All the computational data associated with this study are freely available at the Git repository https://github.com/caneparesearch/NASICON_KMC_paper_data

References

1. Goodenough, J. B. & Park, K.-S. The Li-Ion Rechargeable Battery: A Perspective. *J. Am. Chem. Soc.* **135**, 1167–1176 (2013).
2. Wang, Y. *et al.* Design principles for solid-state lithium superionic conductors. *Nat. Mater.* **14**, 1026–1031 (2015).
3. He, X., Zhu, Y. & Mo, Y. Origin of fast ion diffusion in super-ionic conductors. *Nat. Commun.* **8**, 15893 (2017).
4. Bachman, J. C. *et al.* Inorganic Solid-State Electrolytes for Lithium Batteries: Mechanisms and Properties Governing Ion Conduction. *Chem. Rev.* **116**, 140–162 (2016).
5. Goodenough, J. B. & Kim, Y. Challenges for Rechargeable Li Batteries. *Chem. Mater.* **22**, 587–603 (2010).
6. Famprikis, T., Canepa, P., Dawson, J. A., Islam, M. S. & Masquelier, C. Fundamentals of inorganic solid-state electrolytes for batteries. *Nat. Mater.* **18**, 1278–1291 (2019).
7. Deng, Y. *et al.* Structural and Mechanistic Insights into Fast Lithium-Ion Conduction in Li_4SiO_4 – Li_3PO_4 Solid Electrolytes. *J. Am. Chem. Soc.* **137**, 9136–9145 (2015).
8. Minafra, N., Culver, S. P., Li, C., Senyshyn, A. & Zeier, W. G. Influence of the Lithium Substructure on the Diffusion Pathways and Transport Properties of the Thio-LISICON $\text{Li}_4\text{Ge}_{1-x}\text{Sn}_x\text{S}_4$. *Chem. Mater.* **31**, 3794–3802 (2019).
9. Kamaya, N. *et al.* A lithium superionic conductor. *Nat. Mater.* **10**, 682–686 (2011).
10. Ong, S. P. *et al.* Phase stability, electrochemical stability and ionic conductivity of the $\text{Li}_{10\pm 1}\text{MP}_2\text{X}_{12}$ (M = Ge, Si, Sn, Al or P, and X = O, S or Se) family of superionic conductors. *Energy Env. Sci* **6**, 148–156 (2013).
11. Kuhn, A. *et al.* A new ultrafast superionic Li-conductor: ion dynamics in $\text{Li}_{11}\text{Si}_2\text{PS}_{12}$ and comparison with other tetragonal LGPS-type electrolytes. *Phys Chem Chem Phys* **16**, 14669–14674 (2014).
12. Hori, S. *et al.* Synthesis, structure, and ionic conductivity of solid solution, $\text{Li}_{10+\delta}\text{M}_{1+\delta}\text{P}_{2-\delta}\text{S}_{12}$ (M = Si, Sn). *Faraday Discuss* **176**, 83–94 (2014).
13. Kato, Y. *et al.* High-power all-solid-state batteries using sulfide superionic conductors. *Nat. Energy* **1**, 16030 (2016).
14. Culver, S. P. *et al.* Evidence for a Solid-Electrolyte Inductive Effect in the Superionic Conductor $\text{Li}_{10}\text{Ge}_{1-x}\text{Sn}_x\text{P}_2\text{S}_{12}$. *J. Am. Chem. Soc.* **142**, 21210–21219 (2020).

15. Zhou, L. *et al.* An Entropically Stabilized Fast-Ion Conductor: $\text{Li}_{3.25}[\text{Si}_{0.25}\text{P}_{0.75}]\text{S}_4$. *Chem. Mater.* **31**, 7801–7811 (2019).
16. Minami, T., Hayashi, A. & Tatsumisago, M. Recent progress of glass and glass-ceramics as solid electrolytes for lithium secondary batteries. *Solid State Ion.* **177**, 2715–2720 (2006).
17. Hong, H. Y.-P. Crystal structures and crystal chemistry in the system $\text{Na}_{1+x}\text{Zr}_2\text{Si}_x\text{P}_{3-x}\text{O}_{12}$. *Mater. Res. Bull.* **11**, 173–182 (1976).
18. Goodenough, J. B., Hong, H. Y.-P. & Kafalas, J. A. Fast Na^+ -ion transport in skeleton structures. *Mater. Res. Bull.* **11**, 203–220 (1976).
19. Deng, Z. *et al.* Phase Behavior in Rhombohedral NaSiCON Electrolytes and Electrodes. *Chem. Mater.* **32**, 7908–7920 (2020).
20. Gao, Y. *et al.* Classical and Emerging Characterization Techniques for Investigation of Ion Transport Mechanisms in Crystalline Fast Ionic Conductors. *Chem. Rev.* **120**, 5954–6008 (2020).
21. Zhang, Z. *et al.* New horizons for inorganic solid state ion conductors. *Energy Environ. Sci.* **11**, 1945–1976 (2018).
22. Dawson, J. A., Canepa, P., Famprikis, T., Masquelier, C. & Islam, M. S. Atomic-Scale Influence of Grain Boundaries on Li-Ion Conduction in Solid Electrolytes for All-Solid-State Batteries. *J. Am. Chem. Soc.* **140**, 362–368 (2018).
23. Marcolongo, A. & Marzari, N. Ionic correlations and failure of Nernst-Einstein relation in solid-state electrolytes. *Phys. Rev. Mater.* **1**, 025402 (2017).
24. He, X., Zhu, Y., Epstein, A. & Mo, Y. Statistical variances of diffusional properties from ab initio molecular dynamics simulations. *Npj Comput. Mater.* **4**, 18 (2018).
25. Haarmann, L. & Albe, K. From ionic to superionic conductivity: The influence of cation order on sodium diffusion in $\text{Na}_3\text{Zr}_2\text{Si}_2\text{PO}_{12}$. *Solid State Ion.* **363**, 115604 (2021).
26. Guin, M. & Tietz, F. Survey of the transport properties of sodium superionic conductor materials for use in sodium batteries. *J. Power Sources* **273**, 1056–1064 (2015).
27. Lalère, F. *et al.* An all-solid state NASICON sodium battery operating at 200 °C. *J. Power Sources* **247**, 975–980 (2014).
28. Ma, Q. *et al.* Scandium-Substituted $\text{Na}_3\text{Zr}_2(\text{SiO}_4)_2(\text{PO}_4)$ Prepared by a Solution-Assisted Solid-State Reaction Method as Sodium-Ion Conductors. *Chem. Mater.* **28**, 4821–4828 (2016).
29. Ouyang, B. *et al.* Synthetic accessibility and stability rules of NASICONs. *Nat. Commun.* **12**, 5752 (2021).
30. Boilot, J. P., Collin, G. & Colomban, Ph. Relation structure-fast ion conduction in the NASICON solid solution. *J. Solid State Chem.* **73**, 160–171 (1988).
31. Boilot, J. P., Collin, G. & Colomban, P. Crystal structure of the true nasicon: $\text{Na}_3\text{Zr}_2\text{Si}_2\text{PO}_{12}$. *Mater. Res. Bull.* **22**, 669–676 (1987).
32. Zhang, Z. *et al.* Correlated Migration Invokes Higher Na^+ -Ion Conductivity in NASICON-Type Solid Electrolytes. *Adv. Energy Mater.* **9**, 1902373 (2019).
33. Deng, Y. *et al.* Crystal Structures, Local Atomic Environments, and Ion Diffusion Mechanisms of Scandium-Substituted Sodium Superionic Conductor (NASICON) Solid Electrolytes. *Chem. Mater.* **30**, 2618–2630 (2018).
34. Zou, Z. *et al.* Relationships Between Na^+ Distribution, Concerted Migration, and Diffusion Properties in Rhombohedral NASICON. *Adv. Energy Mater.* **10**, 2001486 (2020).
35. Henkelman, G., Uberuaga, B. P. & Jónsson, H. A climbing image nudged elastic band method for finding saddle points and minimum energy paths. *J. Chem. Phys.* **113**, 9901–9904 (2000).

36. Sun, J., Ruzsinszky, A. & Perdew, J. P. Strongly Constrained and Appropriately Normed Semilocal Density Functional. *Phys. Rev. Lett.* **115**, 036402 (2015).
37. Chen, T., Sai Gautam, G. & Canepa, P. Ionic Transport in Potential Coating Materials for Mg Batteries. *Chem. Mater.* **31**, 8087–8099 (2019).
38. Du, Y. A. & Holzwarth, N. A. W. Mechanisms of Li⁺ diffusion in crystalline γ - and β -Li₃PO₄ electrolytes from first principles. *Phys. Rev. B* **76**, 174302 (2007).
39. Van der Ven, A., Ceder, G., Asta, M. & Tepesch, P. D. First-principles theory of ionic diffusion with nondilute carriers. *Phys. Rev. B* **64**, 184307 (2001).
40. Van der Ven, A., Deng, Z., Banerjee, S. & Ong, S. P. Rechargeable Alkali-Ion Battery Materials: Theory and Computation. *Chem. Rev.* **120**, 6977–7019 (2020).
41. Deng, Y. *et al.* Crystal Structures, Local Atomic Environments, and Ion Diffusion Mechanisms of Scandium-Substituted Sodium Superionic Conductor (NASICON) Solid Electrolytes. *Chem. Mater.* **30**, 2618–2630 (2018).
42. Hayashi, K., Shima, K. & Sugiyama, F. A Mixed Aqueous/Aprotic Sodium/Air Cell Using a NASICON Ceramic Separator. *J. Electrochem. Soc.* **160**, A1467–A1472 (2013).
43. Park, H., Jung, K., Nezafati, M., Kim, C.-S. & Kang, B. Sodium Ion Diffusion in Nasicon (Na₃Zr₂Si₂PO₁₂) Solid Electrolytes: Effects of Excess Sodium. *ACS Appl. Mater. Interfaces* **8**, 27814–27824 (2016).
44. Lunghammer, S. *et al.* Fast Na ion transport triggered by rapid ion exchange on local length scales. *Sci. Rep.* **8**, 11970 (2018).
45. Naqash, S., Tietz, F., Yazhenskikh, E., Müller, M. & Guillon, O. Impact of sodium excess on electrical conductivity of Na₃Zr₂Si₂PO_{12+x}Na₂O ceramics. *Solid State Ion.* **336**, 57–66 (2019).
46. Morgan, B. J. Mechanistic Origin of Superionic Lithium Diffusion in Anion-Disordered Li₆PS₅X Argyrodites. *Chem. Mater.* **33**, 2004–2018 (2021).
47. Morgan, B. J. Lattice-geometry effects in garnet solid electrolytes: a lattice-gas Monte Carlo simulation study. *R. Soc. Open Sci.* **4**, 170824 (2017).
48. Masquelier, C. & Croguennec, L. Polyanionic (Phosphates, Silicates, Sulfates) Frameworks as Electrode Materials for Rechargeable Li (or Na) Batteries. *Chem. Rev.* **113**, 6552–6591 (2013).
49. Xiao, Y. *et al.* Lithium Oxide Superionic Conductors Inspired by Garnet and NASICON Structures. *Adv. Energy Mater.* 2101437 (2021) doi:10.1002/aenm.202101437.
50. Rudolf, P. R., Clearfield, A. & Jorgensen, J. D. A time of flight neutron powder rietveld refinement study at elevated temperature on a monoclinic near-stoichiometric NASICON. *J. Solid State Chem.* **72**, 100–112 (1988).
51. Bukun, N. G. Superionic transitions in NASICON-type solid electrolytes. *Ionics* **2**, 63–68 (1996).
52. von Alpen, U., Bell, M. F. & Wichelhaus, W. Phase transition in nasicon (Na₃Zr₂Si₂PO₁₂). *Mater. Res. Bull.* **14**, 1317–1322 (1979).
53. Jolley, A. G., Taylor, D. D., Schreiber, N. J. & Wachsman, E. D. Structural Investigation of Monoclinic-Rhombohedral Phase Transition in Na₃Zr₂Si₂PO₁₂ and Doped NASICON. *J. Am. Ceram. Soc.* **98**, 2902–2907 (2015).
54. Ma, Q. *et al.* Room temperature demonstration of a sodium superionic conductor with grain conductivity in excess of 0.01 S cm⁻¹ and its primary applications in symmetric battery cells. *J. Mater. Chem. A* **7**, 7766–7776 (2019).
55. Zhu, D., Luo, F., Xie, Z. & Zhou, W. Preparation and characteristic of NASICON ceramics. *Rare Met.* **25**, 39–42 (2006).

56. Chen, D., Luo, F., Zhou, W. & Zhu, D. Influence of Nb⁵⁺, Ti⁴⁺, Y³⁺ and Zn²⁺ doped Na₃Zr₂Si₂PO₁₂ solid electrolyte on its conductivity. *J. Alloys Compd.* **757**, 348–355 (2018).
57. Traversa, E., Aono, H., Sadaoka, Y. & Montanaro, L. Electrical properties of sol–gel processed NASICON having new compositions. *Sens. Actuators B Chem.* **65**, 204–208 (2000).
58. Ladenstein, L. *et al.* On the Dependence of Ionic Transport on Crystal Orientation in Nasicon-Type Solid Electrolytes. *ECS Meet. Abstr.* **MA2020-02**, 946–946 (2020).
59. Grady, Z. M., Tsuji, K., Ndayishimiye, A., Hwan-Seo, J. & Randall, C. A. Densification of a Solid-State NASICON Sodium-Ion Electrolyte Below 400 °C by Cold Sintering With a Fused Hydroxide Solvent. *ACS Appl. Energy Mater.* **3**, 4356–4366 (2020).
60. Perthuis, H. & Colomban, Ph. Sol-gel routes leading to nasicon ceramics. *Ceram. Int.* **12**, 39–52 (1986).
61. Hayashi, K., Shima, K. & Sugiyama, F. A Mixed Aqueous/Aprotic Sodium/Air Cell Using a NASICON Ceramic Separator. *J. Electrochem. Soc.* **160**, A1467–A1472 (2013).
62. Bloembergen, N., Purcell, E. M. & Pound, R. V. Relaxation Effects in Nuclear Magnetic Resonance Absorption. *Phys. Rev.* **73**, 679–712 (1948).
63. Ciucci, F. Modeling electrochemical impedance spectroscopy. *Curr. Opin. Electrochem.* **13**, 132–139 (2019).
64. Kumar, P. P. & Yashonath, S. A Full Interionic Potential for Na_{1+x}Zr₂Si_xP_{3-x}O₁₂ Superionic Conductors. *J. Am. Chem. Soc.* **124**, 3828–3829 (2002).
65. Roy, S. & Kumar, P. P. Influence of Cationic ordering on ion transport in NASICONs: Molecular dynamics study. *Solid State Ion.* **253**, 217–222 (2013).
66. Roy, S. & Padma Kumar, P. Influence of Si/P ordering on Na⁺ transport in NASICONs. *Phys. Chem. Chem. Phys.* **15**, 4965 (2013).
67. Mo, Y., Ong, S. P. & Ceder, G. First Principles Study of the Li₁₀GeP₂S₁₂ Lithium Super Ionic Conductor Material. *Chem. Mater.* **24**, 15–17 (2012).
68. Zhou, M. & Ahmad, A. Synthesis, processing and characterization of nasicon solid electrolytes for CO₂ sensing applications. *Sens. Actuators B Chem.* **122**, 419–426 (2007).
69. Singh, B. *et al.* A chemical map of NaSICON electrode materials for sodium-ion batteries. *J. Mater. Chem. A* **9**, 281–292 (2021).
70. Wang, Z. *et al.* Phase Stability and Sodium-Vacancy Orderings in a NaSICON Electrode. *ArXiv210906997 Cond-Mat* (2021).
71. Jolley, A. G., Cohn, G., Hitz, G. T. & Wachsman, E. D. Improving the ionic conductivity of NASICON through aliovalent cation substitution of Na₃Zr₂Si₂PO₁₂. *Ionics* **21**, 3031–3038 (2015).
72. Miyajima, Y. Solubility range and ionic conductivity of large trivalent ion doped Na_{1+x}M_xZr_{2-x}P₃O₁₂ (M: In, Yb, Er, Y, Dy, Tb, Gd) solid electrolytes. *Solid State Ion.* **124**, 201–211 (1999).
73. Samiee, M. *et al.* Divalent-doped Na₃Zr₂Si₂PO₁₂ natrium superionic conductor: Improving the ionic conductivity via simultaneously optimizing the phase and chemistry of the primary and secondary phases. *J. Power Sources* **347**, 229–237 (2017).
74. Takahashi, T., Kuwabara, K. & Shibata, M. Solid-state ionics - conductivities of Na⁺ ion conductors based on NASICON. *Solid State Ion.* **1**, 163–175 (1980).
75. Shannon, R. D. Revised effective ionic radii and systematic studies of interatomic distances in halides and chalcogenides. *Acta Crystallogr. Sect. A* **32**, 751–767 (1976).
76. Park, H., Kang, M., Park, Y.-C., Jung, K. & Kang, B. Improving ionic conductivity of Nasicon (Na₃Zr₂Si₂PO₁₂) at intermediate temperatures by modifying phase transition behavior. *J. Power Sources* **399**, 329–336 (2018).

77. Kresse, G. & Furthmüller, J. Efficient iterative schemes for ab initio total-energy calculations using a plane-wave basis set. *Phys. Rev. B* **54**, 11169–11186 (1996).
78. Kresse, G. & Furthmüller, J. Efficiency of ab-initio total energy calculations for metals and semiconductors using a plane-wave basis set. *Comput. Mater. Sci.* **6**, 15–50 (1996).
79. Gorai, P., Famprakis, T., Singh, B., Stevanović, V. & Canepa, P. Devil is in the Defects: Electronic Conductivity in Solid Electrolytes. *Chem. Mater.* **33**, 7484–7498 (2021).
80. Chen, T., Sai Gautam, G. & Canepa, P. Ionic Transport in Potential Coating Materials for Mg Batteries. *Chem. Mater.* **31**, 8087–8099 (2019).
81. Boilot, J. P., Salanié, J. P., Desplanches, G. & Le Potier, D. Phase transformation in $\text{Na}_{1+x}\text{Si}_x\text{Zr}_2\text{P}_{3-x}\text{O}_{12}$ compounds. *Mater. Res. Bull.* **14**, 1469–1477 (1979).
82. Ignaszak, A., Pasierb, P., Gajerski, R. & Komornicki, S. Synthesis and properties of Nasicon-type materials. *Thermochim. Acta* **426**, 7–14 (2005).
83. Wang, X., Chen, J., Mao, Z. & Wang, D. Effective resistance to dendrite growth of NASICON solid electrolyte with lower electronic conductivity. *Chem. Eng. J.* **427**, 130899 (2022).
84. Bohnke, O. Conductivity measurements on nasicon and nasicon-modified materials. *Solid State Ion.* **122**, 127–136 (1999).
85. Liu, S. *et al.* Ce-Substituted Nanograin $\text{Na}_3\text{Zr}_2\text{Si}_2\text{PO}_{12}$ Prepared by LF-FSP as Sodium-Ion Conductors. *ACS Appl. Mater. Interfaces* **12**, 3502–3509 (2020).
86. Naqash, S., Ma, Q., Tietz, F. & Guillon, O. $\text{Na}_3\text{Zr}_2(\text{SiO}_4)_2(\text{PO}_4)$ prepared by a solution-assisted solid state reaction. *Solid State Ion.* **302**, 83–91 (2017).
87. Huggins, R. A. Simple method to determine electronic and ionic components of the conductivity in mixed conductors a review. *Ionics* **8**, 300–313 (2002).

Supplementary Files

This is a list of supplementary files associated with this preprint. Click to download.

- [nasionkmcSiforsubmission.pdf](#)